communications physics

A Nature Portfolio journal

Article

https://doi.org/10.1038/s42005-025-02438-x

Extra hole threshold in HfO_2 ferroelectric phase stabilization

Check for updates

Xixiang Jing[1,7], Yuhao Yue[2,7], Shuning Lv[3,7], Kang Jia[1], Kepeng Song[4], Fatoye Sawyerr[1], Qi Hu[3] ✉, Zekun Zhang[1], Shu Shi[5], Shifeng Wen[6], Li-Min Liu[3], Jingsheng Chen[5], Xiaoli Fan[1] ✉, Zheng Wen[2] ✉ & Tengfei Cao[1] ✉

Understanding ferroelectric phase stability in hafnium-based oxides is crucial for high-quality thin-film fabrication and device applications. Multiple strategies stabilize the phase, with evidence highlighting extra holes' key role. However, research on extra holes' impact on ferroelectric phase stabilization remains inadequate. This study combines first-principles calculations with experimental data, identifying a critical extra-hole concentration threshold (0.3 h/f.u.) for HfO_2 ferroelectric phase stabilization. We designed two coordinated experiments to verify the extra-hole threshold in HfO_2. Using $SrRuO_3$ (SRO) as the bottom electrode, we studied three HfO_2 systems (Sm, Eu, and La doped). All systems showed optimal ferroelectric performance at 7.5% doping. Our results also showed that HfO_2 films on Sm-doped ($La_{0.67}Sr_{0.33}MnO_3$) LSMO (5.5% doping) achieve optimal polarization, comparable to SRO (7.5%). These mutually corroborative experimental and theoretical results indicate that the extra-hole threshold optimizes HfO_2 ferroelectric thin film growth and facilitates its electronic device applications.

Hafnium dioxide (HfO_2), a pivotal dielectric material, that has attracted significant attention due to its ferroelectric phase stability, which is a critical research limitation in advanced functional oxides. Recent developments in ultrathin electronic devices have intensified demands for high-performance nanoscale ferroelectrics, driving fundamental investigations into ferroelectricity of HfO_2. Unlike conventional perovskite ferroelectrics[1–4], HfO_2 exhibits exceptional compatibility with complementary metal-oxide-semiconductor (CMOS) processes[5–10] and retains robust ferroelectricity at sub-10 nm thicknesses[11,12]. All these position HfO_2 as a cornerstone for the next-generation nanoelectronics since its first discovery by Boescke et al. in Si-doped hafnium-based systems[13]. However, HfO_2 crystallizes into multiple metastable phases, with phase formation highly sensitive to synthesis protocols and thermal processing[14–16].

Both experimental and theoretical studies reveal that monoclinic phase (M-phase) of HfO_2 is the most stable phase at ambient temperatures[17–19], while tetragonal T-phase emerges at 2000 K[20], and transitions into cubic C-phase at 2870 K[20]. Ferroelectricity in HfO_2 is primarily attributed to the orthorhombic phase (O-phase)[21,22], which is metastable. Consequently, how to stabilize the ferroelectric O-phase of HfO_2 has become a topic of interest in both material science and physics. Several stabilization mechanisms have been proposed, such as the size effect[23–26], strain[27–29], and oxygen vacancies[30–33]. Additionally, there are also numerous studies demonstrating that dopants with large-radius and low-electronegativity could enhance ferroelectric phase stability[34–37]. For example, Chen et al. achieved superior ferroelectric polarization in La-doped $Hf_{0.5}Zr_{0.5}O_2$ films on $La_{0.77}Sr_{0.33}MnO_3$[38]. Tsymbal's work proposed that extra hole doping could stabilize ferroelectric phase by efficiently modulating electrostatic energy[39], and Liu et al. highlighted the critical role of positively charged oxygen vacancies (V_o^{2+}) in reducing phase transition barriers[40]. Collectively, all these studies emphasize the role of elemental doping, charge transfer, and oxygen vacancies in stabilizing ferroelectric phase of HfO_2. And it can be further concluded that the presence of additional holes serves as a unifying factor among all the mechanisms discussed. However, critical knowledge gaps still persist here. For example, how will the synergistic effects of coexisting oxygen vacancies and extra hole doping impact the phase stability? Does a extra optimal hole doping concentration exist for maximizing ferroelectric stability on different substrates? How do substrate-mediated charge transfers (e.g., hole injection *vs.* electron donation) and extra dopants modulate the efficient doping threshold? Here, we systematically address these questions by integrating first-principles calculations with experimental validations. Our findings reveal an extra hole threshold of 0.3 h/f.u. necessary for stabilizing the ferroelectric phase. Notably, this critical threshold demonstrates

[1]Research Center for Advanced Lubrication and Sealing Materials, School of Materials Science and Engineering, Northwestern Polytechnical University, Xi'an, Shaanxi, China. [2]College of Physics, Qingdao University, Qingdao, Shandong, China. [3]School of Physics, Beihang University, Beijing, China. [4]School of Chemistry and Chemical Engineering, Shandong University, Ji'nan, China. [5]Department of Materials Science and Engineering, National University of Singapore, Singapore, Singapore. [6]School of Materials Science and Engineering, Northwestern Polytechnical University, Xi'an, Shaanxi, China. [7]These authors contributed equally: Xixiang Jing, Yuhao Yue, Shuning Lv. ✉e-mail: huqi@buaa.edu.cn; xlfan@nwpu.edu.cn; zwen@qdu.edu.cn; tengfei.cao@nwpu.edu.cn

negligible dependence on oxygen vacancy concentration within the range of 0–1.04 at.%. Experimental confirmation is achieved through the synthesis of HfO_2 thin films doped with various trivalent elements, including Sm, Eu, and La. All dopants exhibit optimal ferroelectric properties at approximately 7.5% doping concentration, which directly demonstrates the extra hole threshold existence. Furthermore, in Sm-doped HfO_2 films epitaxially grown on $La_{0.67}Sr_{0.33}MnO_3$ (LSMO) and $SrRuO_3$ (SRO) bottom electrodes, different optimal extra hole concentrations were observed: 5.5 at% for MnO_2-terminated LSMO (an intrinsic hole-injecting electrode) versus 7.5 at % for SrO-terminated SRO (an electron-donating electrode), which indirectly confirms the existence of the extra hole threshold. Finally, our kinetic phase transition simulations demonstrate that an additional 0.1 h/f.u. of holes reduces the transition barrier from paraelectric M-phase to ferroelectric O-phase by 0.1 eV. This reduction is consistent across transition pathways, regardless of the involvement of the T phase. All these provide a foundational framework for engineering ferroelectric phase in HfO_2-based materials, bridging theoretical predictions with experimental realizations, and paving the way for the scalable synthesis of ferroelectric HfO_2 thin films.

Results and discussion

Theoretical prediction of the existence of extra hole threshold

The structures of paraelectric M-phase and ferroelectric O-phase of HfO_2 are presented in Fig. 1a, b, where the M-phase is the energetic ground state of HfO_2. The O-phase, widely acknowledged as the ferroelectric polarization phase, exists as a metastable structure with an energy 0.08 eV/f.u. higher than the M-phase under defect-free and charge-undoped conditions. Both ferroelectric O-phase and paraelectric M-phase contain two distinct oxygen sublattices: one with three-coordinated oxygen atoms (O_{III}) bonded to three Hf atoms and the other with four-coordinated oxygen atoms (O_{IV}) bonded to four Hf atoms. These are denoted by yellow and red solid circles in Fig. 1, respectively. For HfO_2 samples, the formation of oxygen vacancies may occupy two different sublattices, resulting in the formation of four-coordinated (VO_{IV}) defects or three-coordinated (VO_{III}) defects, respectively. This study systematically investigates extrinsic extra hole doping effects on relative phase stabilities between O- and M-phase under varying concentrations of VO_{III} or VO_{IV}. As illustrated in Fig. 1c, d, extra hole and oxygen vacancies exhibit different modulation effects on static stabilities of the O- and M-phase.

Firstly, in the absence of oxygen vacancies (VO = 0.0%), extra hole doping alone can stabilize the ferroelectric O-phase. The gradual increase in extra hole doping concentration reduces the energy difference between the O- and M-phase, ultimately leading to a reversal of their relative stability when extra hole concentrations exceed 0.2 h/f.u., and making the O-phase energetically favorable. In contrast, oxygen vacancies alone exhibit weaker modulation effects on relatively static stabilities of the O- and M-phase. Thus, without extrinsic hole doping or under low extra hole doping

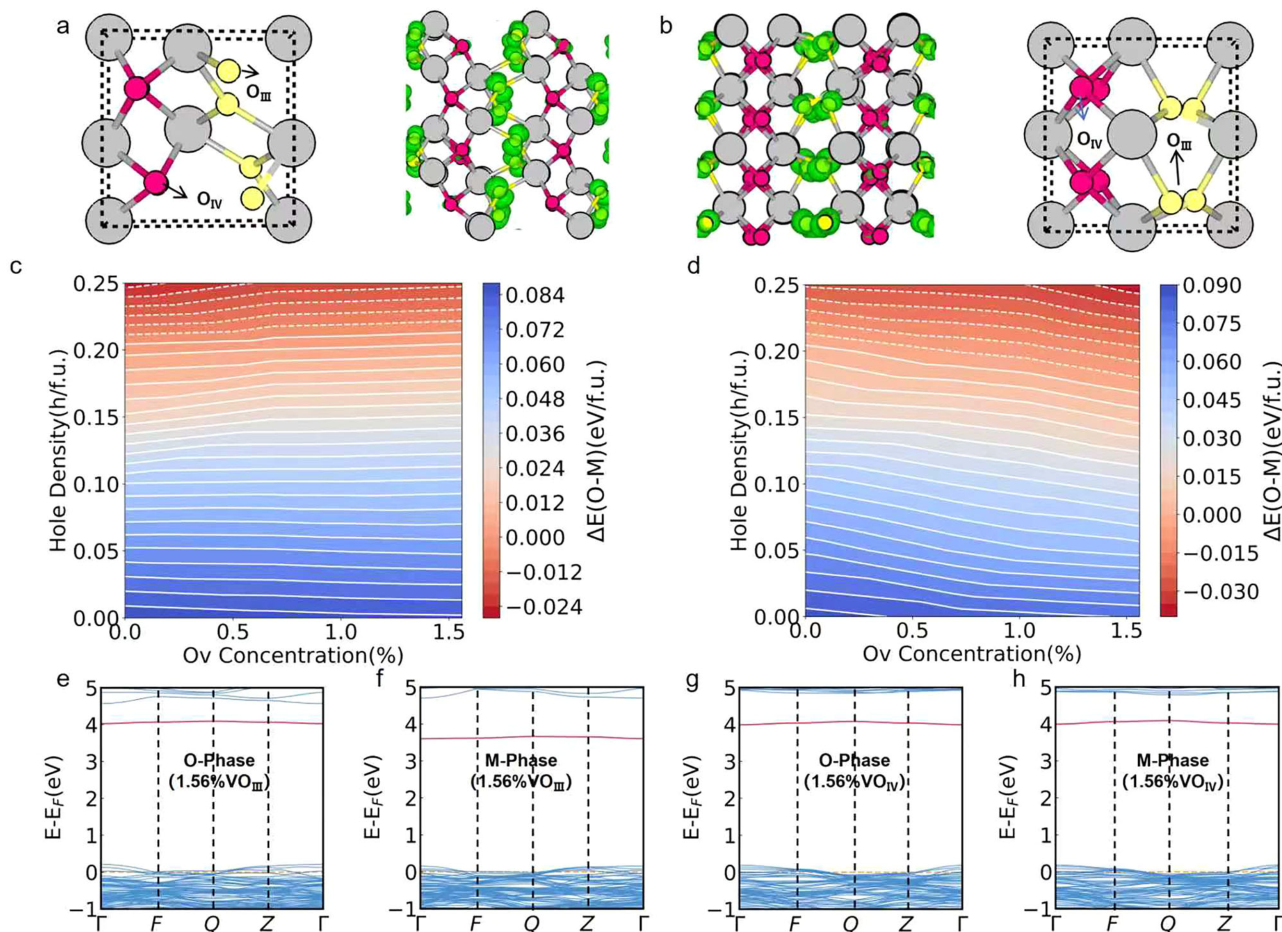

Fig. 1 | Configurations and band structures of HfO_2 phases. a Crystal structures of paraelectric monoclinic (*M*-phase), and (**b**) ferroelectric orthorhombic (*O*-phase) phase. Hafnium (Hf) atoms are represented by gray spheres, and oxygen atoms are color-coded by coordination: red spheres denote fourfold-coordinated oxygen (O_{IV}, bonded to four Hf atoms), and yellow spheres indicate threefold-coordinated oxygen (O_{III}, bonded to three Hf atoms). The spatial distribution of excess extra holes in the HfO_2 lattice is visualized as green iso-surfaces (1/10 of the maximum value). Oxygen vacancies located at threefold-coordinated (**c**) and fourfold-coordinated (**d**) oxygen lattice sites, respectively, demonstrate the modulation effect of vacancy-hole couplings on the relative stability between ferroelectric *O*-phase and paraelectric *M*-phase. **e**–**h** Band structures of *M*-phase and *O*-phase systems containing oxygen vacancies at tetragonal-coordinated (VO_{IV}) and trigonal-coordinated (VO_{III}) oxygen lattice sites, the red curve represents the defect energy level where oxygen vacancies are located.

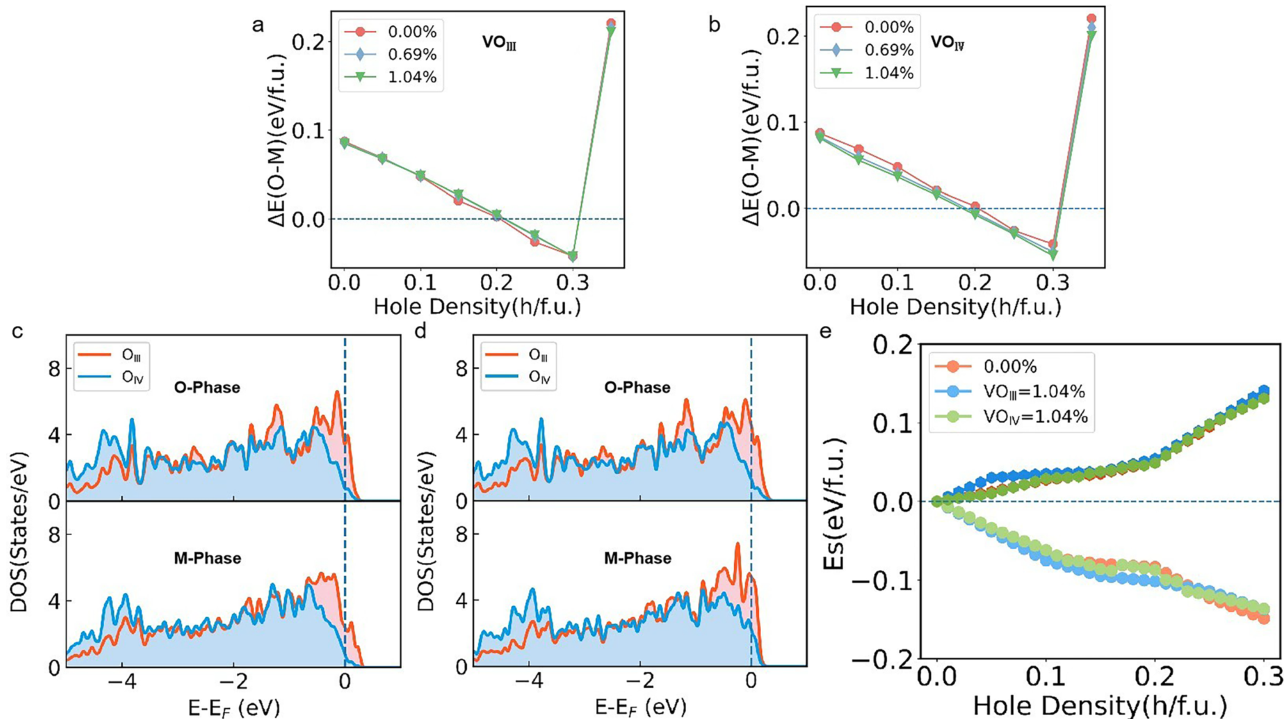

Fig. 2 | Extra Hole doping modulation effects on phase stability and related electronic structures. Optimal extra hole doping concentrations for stabilizing the O-phase under varying concentrations of threefold-coordinated oxygen vacancy (VO_{III}) (**a**) and fourfold-coordinated oxygen vacancy (VO_{IV}) (**b**). Density of states (DOS) of O-, M-phase (VO = 0.00%) under 0.2 h/f.u. (**c**) and 0.3 h/f.u. **d** Extra hole doping concentration. **e** Evolution of electrostatic energy (Es) in the HfO_2 matrix under varying extra hole doping concentrations and with either no (0.00%) or 1.04% concentrations of oxygen vacancies at threefold-coordinated (VO_{III}) and fourfold-coordinated (VO_{IV}) oxygen sublattices. The aforementioned results unambiguously demonstrate that additional hole doping effectively stabilizes ferroelectric phase of HfO_2, irrespective of the presence of oxygen vacancies.

concentrations (<0.2 h/f.u.), varying oxygen vacancy concentrations fails to substantially alter the energy hierarchy or statically stabilize the O-phase as the ground state. Even under high oxygen vacancy concentrations, the stabilization of O-phase still requires critical extra hole doping, specifically 0.2 h/f.u. at a 1.0% oxygen vacancy concentration, and 0.16 h/f.u. at a 1.5% oxygen vacancy concentration, respectively. To further elucidate the cooperative effects of oxygen vacancies and extra hole distribution on phase stabilities, the spatial localization of extra holes in HfO_2 matrix was initially analyzed. Figure 1e–h present band structures of systems containing both oxygen vacancies (O_{III} or O_{IV} sites) and 0.2 h/f.u. concentration of extra holes in the matrix. The band structures show that the localized unoccupied states associated with oxygen vacancies were situated near the conduction band minimum (CBM) within the bandgap. Notably, extrinsic holes predominantly occupy the valence band maximum (VBM) rather than vacancy-induced band-gap states, mirroring the behavior of defect-free HfO_2 systems[41]. Furthermore, asymmetric extra hole distribution occurs on the O_{III} and O_{IV} sublattices because of different orbital contributions from oxygen atoms in the O_{III} and O_{IV} sublattices at the VBM (Fig. 1a, b). The introduction of extra holes, governed by doping concentrations and the coordination environment of oxygen sublattices, critically modulates the relative stability between metastable phases in HfO_2. All these underpin the non-equivalent stabilization effects of oxygen vacancy and extra holes on the stabilization of ferroelectric O-phase.

To further show that there is a universal extra hole threshold in ferroelectric phase stabilization, Fig. 2 shows the switching point of extra hole concentrations in HfO_2 matrix. It is worth noting that we did not consider the common tetragonal T-phase, but instead focused solely on the relative stability analysis of the M-phase and O-phase. The reason is that the tetragonal T-phase exhibits extremely poor tolerance to extra holes. For a perfect T-phase crystal, when the extra hole concentration exceeds 0.2 h/f.u., the symmetry of the tetragonal T-phase will be disrupted and transformed into the cubic C-phase, thereby losing its comparative significance. Conversely, although the T-phase can maintain its symmetry, it remains in a high-energy state when the extra hole concentration is below 0.2 h/f.u. Therefore, the T-phase is not considered in our work. It can be observed that, a universal extra hole threshold exists for pristine lattices (0.00%) and oxygen-deficient systems (e.g., 0.69% or 1.04% concentration of oxygen vacancies) (Fig. 2a, b). Specifically, within the oxygen vacancy concentration range of 0.00%-1.04%, both VO_{III} and VO_{IV} systems exhibit an identical extra hole threshold of 0.3 h/f.u., demonstrating the weak dependence of threshold on oxygen vacancy concentrations. However, when oxygen vacancy concentration reaches 1.56%, exceeding this range, the threshold remains unchanged at 0.3 h/f.u. for VO_{III}, but it decreases to 0.25 h/f.u. in VO_{IV} system (Fig. S1a, b). These findings confirm that although the optimal extra hole doping concentrations may vary across different systems, a extra hole threshold persistently exists during the stabilization process of the O-phase. When extra hole concentrations fall below the threshold, the introduction of additional holes stabilizes the ferroelectric O-phase. However, once the number of extra holes exceeds the threshold, they begin to destabilize it (Fig. 2a, b). The density of states (DOS) of O-, M-phase (VO = 0.00%) under 0.2 h/f.u. and 0.3 h/f.u. extra hole doping concentration are given in Fig. 2c, d, respectively. The $2p$ valence states of O_{III} are closer to the Fermi level, and also have more states localized nearby the Fermi level with respect to O_{IV}. Consequently, extra holes preferentially occupy O_{III} sites at low concentrations (see Fig. 2c). However, as the extra hole doping concentration increases, extra holes start to populate the O_{IV} sites (Fig. 2d). The above-mentioned extra hole threshold in HfO_2 arises from the competing occupancy of doping extra holes in the O_{III} and O_{IV} sublattices. Furthermore, the DOS of the first-neighbor O_{III} and O_{IV} atoms adjacent oxygen vacancies under extra hole doping concentrations of 0.2 h/f.u. and 0.3 h/f.u are also calculated (Fig. S2). The results reveals that the extra hole occupancy sites of these oxygen atoms exhibit remarkable

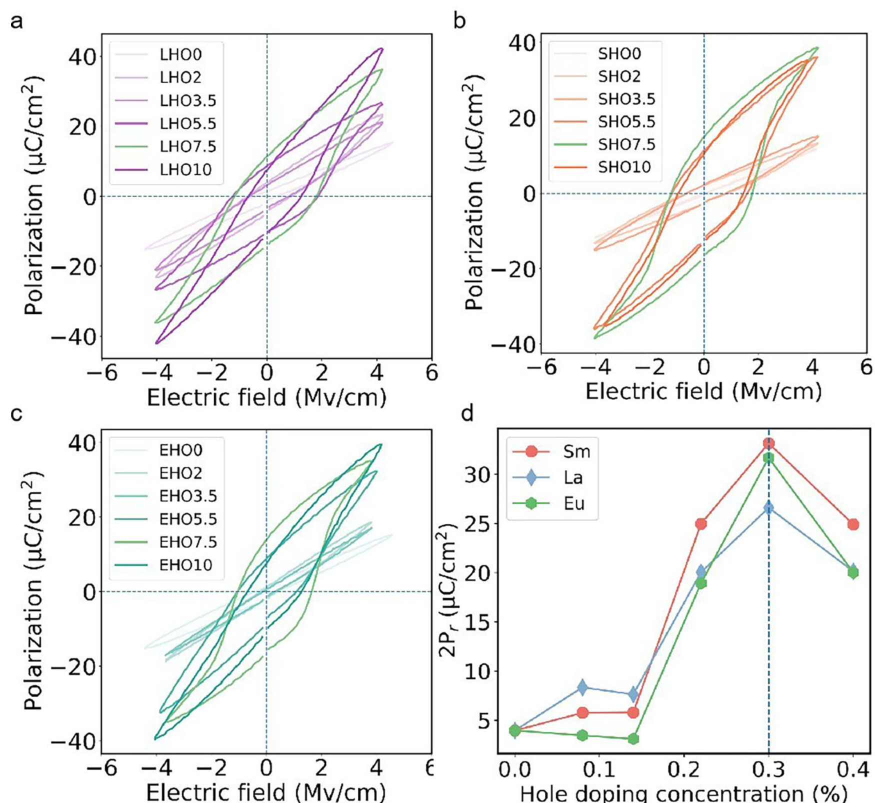

Fig. 3 | Ferroelectric Characterization of Extra Hole-Doped (Sm, La, Eu) HfO_2 Thin Films Epitaxially Grown on $SrRuO_3$ Bottom Electrodes. **a–c** Polarization-electric field (P-E) hysteresis loops for Sm-, La-, and Eu-doped systems under a doping concentration gradient of 0.0–10 at.%. The measurement frequency is 10 kHz. **d** Quantitative correlation between doping concentrations of extra hole-doped agents and remnant polarization ($2P_r$), illustrating the structure-property relationship.

consistency with those in the pristine crystal, predominantly occupying the O_{III} sites. Therefore, with the progressive increase in additional hole doping concentration, extra holes begin to occupy O_{IV} sites in a gradual manner. This phenomenon demonstrates the weak interaction between extra holes and oxygen vacancies in HfO_2 matrix (Fig. S2). To understand the extra hole threshold in HfO_2, the electrostatic energies of pristine HfO_2, 1.04% VO_{III}, and 1.04% VO_{IV} systems are further calculated, and all results are given in Fig. 2e. The results show that when extra holes occupy the O_{III} sites, the electrostatic energy of the M-phase is higher than that of the O-phase at equivalent doping levels. Also, when additional holes are located on the O_{IV} sites, the electrostatic energy of the M-phase is lower than that of the O-phase. Therefore, the extra hole threshold for the stabilization of the O-phase arises from the competing occupancy of extra holes on the O_{III} and O_{IV} sublattices. At low concentrations, extra holes predominantly occupy the O_{III} sites, leading to a gradual stabilization of the O-phase as extra hole doping concentrations increase. This process continues until the optimal concentration is reached, at which point the O-phase is fully stabilized and the energy difference between the O-phase and the M-phase is maximized. Beyond this point, the further introduction of extra holes into the HfO_2 matrix increases the occupancy of extra holes in the O_{IV} sublattices. The resultant increase in electrostatic energy destabilizes the O-phase, making it energetically unfavorable. Furthermore, oxygen vacancy in O_{III} and O_{IV} sublattice could impact the optimal extra hole concentrations for the O-phase stabilization. Interestingly, VO_{III} vacancies have only minimal impacts on the optimal extra hole doping concentrations, whereas VO_{IV} vacancies at 1.56% reduce the optimal extra hole doping concentration from 0.3 to 0.25 h/f.u. This discrepancy arises from the fact that the VO_{IV} could induce larger lattice distortion than VO_{III}, which could be proven by their different lattice parameter variations (Fig. S3). VO_{IV} vacancies significantly shorten the lattice constants along the *b*-axis under extra hole doping, while VO_{III} vacancies exhibit negligible impacts on HfO_2 structure. These different lattice variations modify electrostatic energies of related structures (Fig. S1c), which ultimately control the variation of optimal extra hole doping concentrations.

Experimental verification of the existence of extra hole threshold

To experimentally validate the proposed universal extra hole threshold for HfO_2 ferroelectric phase stabilization, we have designed two mutually coordinated experiments: Firstly, we employed lattice-matched $SrRuO_3$ (SRO) bottom electrode, and incorporated Sm, Eu, and La as extra hole-doping agents to analyze different dopant effects on ferroelectric phase stabilities. Then we maintained Sm as the only specific extra hole-doping agent and analyzed two distinct electrode materials effects on phase stabilities of HfO_2: $La_{0.67}Sr_{0.33}MnO_3$ (LSMO) and SRO. The LSMO could pre-injected extra holes to HfO_2 matrix, while the SRO could introduce electrons to it.

The as-grown HfO_2 thin films with varying compositions were experimentally characterized in accordance with the aforementioned design. Figure S7 shows the HAADF-STEM image and its magnified view of the SHO5.5/SRO thin-film heterostructure, revealing an O-phase with (002) orientation. Figure S8 and Fig. 4c shows the XRD pattern of the HfO_2/SRO heterostructure doped with La, Sm, and Eu concentrations ranging from 0 at % to 10 at% (mole ratio). It can be seen that the three systems follow similar phase transition paths. As the doping content increases from 0 at% to 10 at %, the proportion of the ferroelectric phase is gradually increasing. The ferroelectric polarization of HfO_2 films achieves its maximum value at a extra hole doping concentration of 7.5% for all dopants, including Sm, La, and Eu. All related results are given in Fig. 3a–c, respectively, where polarization-electric field (P-E) hysteresis measurements revealed a consistent concentration-dependent behavior across all three doping systems. The remnant polarization (P_r) initially increases and then decreases with increasing doping concentration, which aligns well with the phase transition behavior. In order to observe the relationship between the doping concentration and the remnant polarization more intuitively, the $2P_r$ are plotted in Fig. 3d. Under the action of the SRO bottom electrode, all three doping systems achieved the peaked polarization value of P_r around doping concentration of 7.5% as shown in Fig. 2a, b. This universal trend indicates the existence of a unified critical doping threshold under identical growth conditions and bottom electrodes constraints, independent of dopant

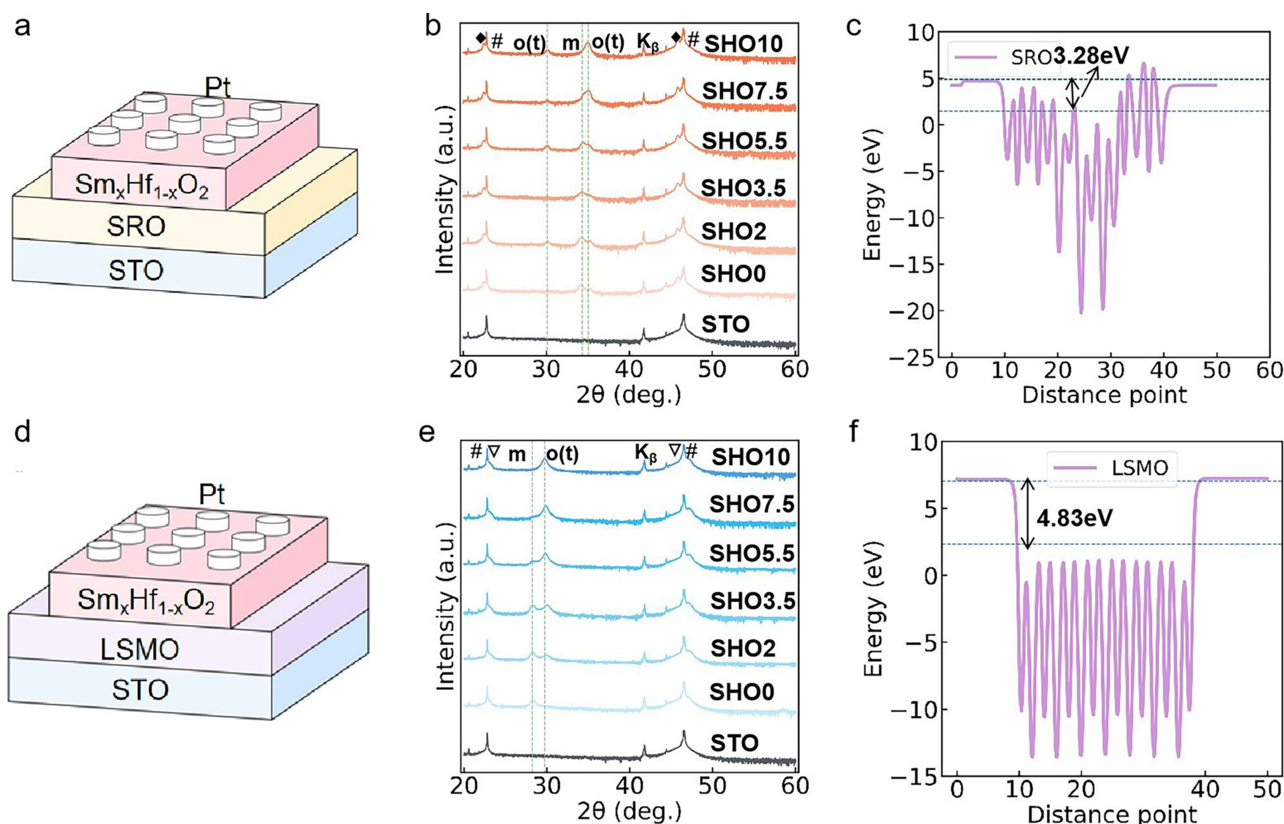

Fig. 4 | Comparative study of Sm-doped HfO_2 ferroelectric thin films epitaxially grown on SRO($SrRuO_3$) and LSMO($La_{0.67}Sr_{0.33}MnO_3$) bottom electrodes. **a**, **b** Schematic illustrations of Sm-doped HfO_2 ferroelectric thin films grown on SRO and LSMO bottom electrodes; (**c**, **d**) XRD(X-ray Diffraction) patterns of films with varying Sm doping concentrations (0–10 at.%) on respective bottom electrodes. **e**, **f** The interfacial electrostatic potential distributions on the SrO-terminated SRO surface and the MnO_2-terminated LSMO surface, where the distance between the blue dashed lines represents the magnitude of the work function (the difference between the vacuum level and the Fermi level), and the orange dashed lines denote the corresponding interface work functions of HfO_2 films with distinct crystallographic orientations.

species. To elucidate the underlying mechanism, XPS characterization of optimally doped samples (Fig. S4) showed a systematic shift in *O1s* binding energy from 530 eV to 531.5 eV. Theoretical analysis employing a surface defect model (See Fig. S5 for details) demonstrated that oxygen vacancy-rich systems exhibit *O1s* energy shifts exceeding 2 eV, while defect-free lattices show shifts of ~1.6 eV (Fig. S6). The experimentally observed 1.5 eV shift closely aligns with theoretical predictions for intact lattices (relative error < 7%), confirming significantly reduced oxygen vacancy concentrations in optimized films. This observation perfectly aligns with above simulations that a universal extra hole-doping thresholds exists in ferroelectric phase stabilization within certain oxygen vacancy concentration ranges.

After successfully establishing the threshold trend for the extra hole-doped system on the homogeneous bottom electrodes, we further utilized interface charge engineering to deeply explore the modulation mechanism of the bottom electrodes on the ferroelectric properties of Sm-doped HfO_2. Precisely, we compared the work functions of Sm-doped HfO_2 ferroelectric thin films with different orientations grown on two different bottom electrodes (SRO and LSMO) to determine the charge transport characteristics of the two bottom electrodes. The schematic diagram of its principle is shown in Fig. 4a, b. For the LSMO bottom electrodes, in order to obtain the MnO_2 termination for charge exchange between LSMO and HfO_2 ferroelectric thin films, the STO substrate was firstly treated by hydrofluoric acid etching process[42]. As given in Fig. S11, the etched STO surface is TiO_2-terminated and exhibits distinct step structures, and the MnO_2-terminated LSMO buffer-layer are further grown on STO for the further growth of epitaxial HfO_2 films. For the SRO bottom electrode, it is reported that the RuO_2-termination has a higher surface energy than the SrO-termination[43]. The RuO_2 atomic layer is easily decomposed because of the volatile character of the Ru element. Therefore, we can obtain the SrO-terminated SRO through high temperature treatments (775 °C), and our XRD characterization clearly show that the SrO-terminated SRO induced the growth of HfO_2 ferroelectric thin films along the (002) orientation (see Fig. 4c). Furthermore, the MnO_2-terminated LSMO bottom electrodes promoted the growth of the HfO_2 ferroelectric thin film along the (111) orientation (see Fig. 4d). To distinguish the volume fraction of each phase, Bragg reflections of the SHO thin films are fitted into a number of Gaussian peaks (Figure S12). The extracted phase volume fractions are plotted in Fig. S13 for clarity. For the SRO electrode, when the Sm concentration is 7.5%, the volume fraction of the O-phase reaches a peak of 64%, and it is mainly composed of O_{002}. However, for the LSMO electrode, when the Sm concentration is 5.5%, the proportion of the o phase reaches the maximum, and only the O_{111} form exists. To analyze the charge exchange between HfO_2 film, SRO, and LSMO, we further calculated their surface work functions, respectively. The surface work function of HfO_2 in (100) direction is calculated to be 6.47 eV (Fig. S9a). At the same time, the work function of the SrO termination surface of the SRO bottom electrode is 3.28 eV (Fig. 4e), which indicates that the SRO bottom electrode will inject electrons to the HfO_2 films. On the other hand, the surface work function of the MnO_2-terminated LSMO bottom electrode is 4.83 eV (Fig. 4f), and it is lower than the (111) surface of HfO_2 films (2.97 eV), which demonstrate that the LSMO could donate extra holes to HfO_2 films (Figure S9b). After determining the interface charge exchange characteristics of the two different substrates, we measured the hysteresis loops of HfO_2 ferroelectric thin films doped with Sm at different concentrations. The measurement results indicate that, for LSMO bottom electrodes exhibiting a extra hole pre-doping effect, the optimal Sm doping concentration required to achieve the best ferroelectric performance

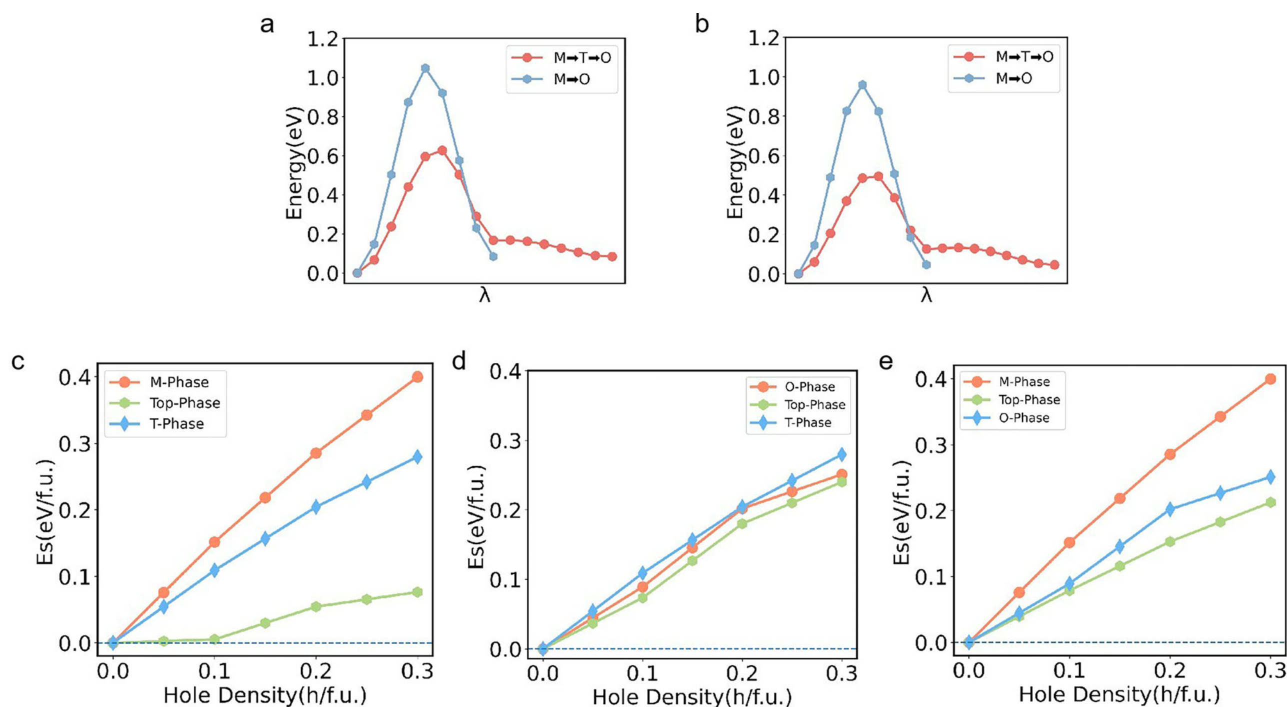

Fig. 5 | Switching barriers of and electrostatic energy of HfO_2. a Phase transition pathways between paraelectric M-phase, ferroelectric O-phase, and intermediate tetragonal (T) phase under (**a**) zero extra hole doping and (**b**) 0.1 h/f.u. doping (0.1 extra holes per formula unit). **c**–**e** The variation of the electrostatic energy at energy maximal with the initial and final phases in three distinct phase transition paths (M-T, T-O, and M-O) with respect to the excess extra hole concentration.

decreases to 5.5 at.% (Fig. S10)—2% lower than the 7.5 at.% observed in SRO bottom electrode systems. All these can be attributed to the fact that extra hole injection effect at the $Sm_xHf_{1-x}O_2$/LSMO interface has already introduced extra holes in HfO_2 matrix, which reduces the necessary extra hole concentration threshold. This result also verifies the key role of the extra hole threshold in HfO_2 ferroelectric phase stabilization. It should be notified that these is discrepancy in the hole doping concentrations between the DFT calculations and experimental measurements, it may come from the fact that only an idealized charge doping environment is considered in the simulations, whereas in experiments, additional factors such as film thickness, strain, defects, and boundary effects may all influence the stabilization of the orthorhombic phase.

Additional holes reduce the M-O phase transition barrier

Apart from the universal extra hole threshold on the static phase stability of ferroelectric O-phase, we further investigated their influence on the energy barriers controlling the phase transitions from O-phase to M-phase in HfO_2. It is already known that the tetragonal T-phase with $P4_2/nmc$ symmetry is the critical intermediate structure during the M-to-O phase transformations. Therefore, we systematically calculated the direct M to O-phase transition barriers and the sequential M- to T- to O-phase transitions mediated by the intermediate T-phase (Fig. 5a). The direct M- to O-phase transition exhibits a substantially higher energy barrier of 1.10 eV, compared to the M-T-O pathway (0.6 eV), confirming the critical role of the *T*-phase in facilitating phase transformations. Subsequent analysis revealed that extra hole doping could significantly modulates these transition barriers (Fig. 5b). Under 0.1 h/f.u. extra hole doping concentration, the direct M- to O-phase transition barrier decreases from 1.10 eV to 1.00 eV, and the M-T-O transition barrier reduces from 0.6 eV to 0.5 eV. These results conclusively demonstrate that both extra hole doping and its synergistic coupling with oxygen vacancies substantially lower the phase transition barriers between paraelectric and ferroelectric phases, thereby thermodynamically favoring the stabilization of ferroelectric O-phase. The barrier-lowering mechanism can also be elucidated through electrostatic energy variations induced by extra hole redistributions (Fig. 5c–e). Taking the M-phase to O-phase transition as an example, we computed the electrostatic energies of the M-phase and the saddle-point (S) configuration along the transition path under equivalent extra hole concentrations. The calculations reveal significantly higher electrostatic energy in the M-phase compared to the S-configuration, and it effectively reduces the energy difference between the M-phase and the saddle state, which consequently lowers the M- to O-phase transition barrier. This electrostatic modulation mechanism provides fundamental insights into the enhanced phase transformability mediated by charge carrier engineering in HfO_2-based ferroelectric systems.

Conclusions

The extra hole threshold in stabilizing the ferroelectric O-phase of HfO_2 is systematically investigated by combining first-principles calculations and experimental measurements. Our results demonstrate that there is always a extra hole doping threshold existing for stabilizing HfO_2 ferroelectric phase, irrespective of oxygen vacancies. This extra hole doping threshold arises from the competitive distribution of extra holes in three-coordinated and four-coordinated oxygen sites, controlled by distinct energy level alignments of oxygen 2*p* orbitals. The phenomenon can be rationalized through extra hole concentration-dependent variations in electrostatic energy caused by differential extra hole distributions within the HfO_2 matrix. Building upon theoretical predictions, we successfully fabricated stable ferroelectric HfO_2 thin films on $La_{0.67}Sr_{0.33}MnO_3$ and $SrRuO_3$ substrates, achieving optimal extra hole doping concentrations through 5.5% and 7.5% Sm doping, respectively. Theoretical analysis indicates that the optimal Sm doping levels are determined by synergistic effects between efficient charge transfer at the HfO_2/substrate interface ($La_{0.67}Sr_{0.33}MnO_3$ or $SrRuO_3$) and Sm-induced extra hole doping. Furthermore, phase transition calculations demonstrate significant reductions in energy barriers for both direct monoclinic (M)-to-orthorhombic (O) and M→tetragonal (T) → O transformations under extra hole doping conditions. These computational results further corroborate the essential role of extra hole doping in facilitating the formation and stabilization of ferroelectric O-phase HfO_2. This comprehensive study not only elucidates the fundamental mechanism of extra hole-mediated stabilization in HfO_2 ferroelectrics, but also provides crucial guidance for

developing high-precision, large-scale oxide thin films with enhanced functional properties.

Methods

Computational methods

We performed density functional theory (DFT) calculations using the Vienna Ab-initio Simulation Package (VASP)[44]. The energy cutoff value of the plane wave was set to 500 eV. The energy convergence threshold for the self-consistent loop was set to 10^{-5} eV. For structural optimization, the force convergence was set to 0.001 eV/angstrom and the Projector Augmented Wave (PAW) method was used to describe electron-ion interactions[45]. We perform supercell calculations for the O-phase, M-phase, and T-phase with different oxygen vacancy concentrations by expanding the unit cell as follows: $2\times3\times3$ (0.59%), $2\times2\times3$ (1.04%), $2\times2\times2$ (1.56%). In the irreducible Brillouin zone, the corresponding k-point meshes of $3\times2\times2$, $2\times3\times2$ and $3\times3\times3$ are used for different supercells, respectively. To simulate charge doping, we changed the total number of electrons in the unit cell in a uniform charge background and optimized the charge structure. Additionally, Quantum Espresso (QE)[46] was utilized for XPS simulations[47] using the Car-Parrinello Molecular Dynamics (CPMD) method[48], with the plane-wave cutoff energy set to 60.0 Ry. In electron dynamics, the electron mass and electron damping were set to 500.0 and 0.01, respectively. Ion dynamics employed the Verlet algorithm for simulating ion motions. Ultrasoft pseudopotentials were adopted to balance computational accuracy and efficiency[49]. All calculations were performed using the Generalized Gradient Approximation (GGA)[50] with the Perdew-Burke-Ernzerhof (PBE) functional to describe electron exchange-correlation effects. Finally, the climbing image nudged elastic band (CI-NEB)[51] method was applied to calculate the energy barriers during the phase transition processes among the ferroelectric O phase, the monoclinic M phase, and the tetragonal T phase, with the number of transition states set to 7 to fully characterize the entire phase Transition pathway.

In this study, the core-shell model was employed to simulate the electrostatic interactions among doped charges in HfO_2. First of all, the atomic structure of HfO_2 was fully optimized based on density functional theory (DFT), and periodic boundary conditions were applied to ensure the accuracy of the calculation. Within the framework of the core-shell model, each atomic site contains an ionic charge (Q_i) fixed at its equilibrium position, and an electronic charge (q_i) bound to its corresponding ionic site. Here, the ionic charge is treated as a point charge. The electronic charge (q_i) is carefully adjusted to accurately simulate the extra hole distribution on the oxygen sub-lattice, and is broadened by a Gaussian distribution function with a width of σ_i to better conform to the actual physical situation. It is worth emphasizing that the parameter settings used in this study are based on our previous work[39], and have successfully reproduced the dielectric constants and energy characteristics of both polar and non-polar phases of HfO_2 in its charge-neutral optimized state, thereby ensuring the reliability and validity of the simulation results. Finally, the electrostatic energy was precisely calculated using the Ewald method (As shown below).

$$
\begin{aligned}
U_{Ewald} = & \frac{1}{2}\sum_{n}\sum_{i}^{N+n}\sum_{j\neq i}^{N+n}\frac{q_i q_j}{\left|\boldsymbol{r_i}-\boldsymbol{r_j}-\boldsymbol{R_n}\right|}\operatorname{erfc}\left[\frac{\boldsymbol{r_i}-\boldsymbol{r_j}-\boldsymbol{R_n}}{\sqrt{2}\sigma_{\mathrm{ew}}}\right] \\
& +\frac{2\pi}{V}\sum_{G\neq 0}\frac{\exp\left(-\frac{\sigma^2_{\mathrm{ew}}G^2}{2}\right)}{G^2}|S(G)|^2-\frac{1}{\sqrt{2\pi}\sigma_{\mathrm{ew}}}\sum_{i}^{N+n}q_i^2+\sum_{i}^{n}\frac{q_i Q_i}{\Delta s_i}\operatorname{erf}\left(\frac{\Delta s_i}{\sqrt{2}\sigma_{\mathrm{ew}}}\right) \\
& -\sum_{n}\sum_{i}^{N}\sum_{j}^{N}\frac{q_i Q_j}{|\boldsymbol{s_i}-\boldsymbol{r_j}-\boldsymbol{R_n}|}\operatorname{erfc}\left[\frac{\boldsymbol{s_i}-\boldsymbol{r_j}-\boldsymbol{R_n}}{\sqrt{2}\sigma_i}\right] \\
& -\sum_{n}\sum_{i}^{N}\sum_{j\neq i}^{N}\frac{q_i q_j}{|\boldsymbol{s_i}-\boldsymbol{r_j}-\boldsymbol{R_n}|}\operatorname{erfc}\left[\frac{\boldsymbol{s_i}-\boldsymbol{r_j}-\boldsymbol{R_n}}{\sqrt{2\left(\sigma_i^2-\sigma_j^2\right)}}\right]
\end{aligned}
$$

Sample preparation

Experiment I, Sm:HfO_2, La:HfO_2, and Eu:HfO_2 thin films, as well as SRO bottom electrodes were deposited on (001)-orientated STO substrates by PLD using a KrF excimer laser. The SRO, about 32 nm in thickness, was deposited at a laser energy density of ~3.0 J/cm^2 with a repetition rate of 8 Hz, keeping the oxygen pressure at 0.1 mbar. The substrate temperature was controlled to 775 °C for achieving SrO-dominated surface. The Sm:HfO_2, La:HfO_2, and Eu:HfO_2 were deposited at a laser energy density of ~2.5 J/cm^2 with a repetition rate of 4 Hz, keeping the substrate at 600 °C and the oxygen pressure at 0.1 mbar. The thin-film thickness was controlled by counting the laser pulse number. The HfO_2-based thin-film heterostructures were post-annealed in a tube furnace at 700 °C for 30 min in flowing O_2. Pt top electrodes of ~30 μm in diameter and ~50 nm in thickness were deposited by a DC magnetron sputtering through a shadow mask. Experiment II, Sm:HfO_2 thin films, as well as LSMO bottom electrodes were deposited on (001)-orientated STO substrates by PLD using a KrF excimer laser. The LSMO thin films were deposited at a laser energy density of ~3.2 J/cm^2 with a repetition rate of 2 Hz, keeping the substrate at 700 °C and the oxygen pressure at 0.2 mbar. In order to control the interface termination, STO substrates were treated with a buffered hydrofluoric acid etching process followed by thermal treatment at 1050 °C for 1 h to get a TiO_2-terminated surface before growth. The experiment of the Sm:HfO_2 thin film and Pt top electrode are the same as those in Experiment I.

Characterization

XRD was performed on a Rigaku Smart Lab X-ray diffractometer with Cu Kα radiation. Ferroelectric hysteresis loops were measured by a Radiant Premier II ferroelectric tester. XPS was performed on a Thermo ESCALAB 250Xi and the binding energy was calibrated by setting the C 1 s as 284.6 eV.

Data availability

The authors declare that the data that support the findings of this study are available within the article. All other relevant data are available from the corresponding authors upon request.

Received: 16 June 2025; Accepted: 16 November 2025;
Published online: 24 December 2025

References

1. Zhang, D. et al. Diversiform Sensors and Sensing Systems Driven by Triboelectric and Piezoelectric Nanogenerators. *Coord. Chem. Rev.* **427**, 213597 (2021).
2. Beyer, S. et al. Wafer-scale integration of double gated WS_2-transistors in 300mm Si CMOS fab. *Proc. IEEE Conf. Ser.* 1–4 (2020).
3. Mohith, S., Upadhya, A. R., Navin, K. P., Kulkarni, S. & Rao, M. Recent Trends in Piezoelectric Actuators for Precision Motion and Their Applications: A Review. *Smart Mater. Struct.* **30**, 013002 (2020).
4. Francois, T. et al. Ferroelectric HfO_2 for memory applications: impact of Si doping technique and bias pulse engineering on switching performance. *Proc. IEEE Conf. Ser.* 15.17.11–15.17.14 (2019).
5. Ali, F. et al. Fluorite-Structured Ferroelectric and Antiferroelectric Materials: A Gateway of Miniaturized Electronic Devices. *Adv. Funct. Mater.* **32**, 2201737 (2022).
6. Luo, Q. et al. A Highly CMOS Compatible Hafnia-Based Ferroelectric Diode. *Nat. Commun.* **11**, 1391 (2020).
7. Park, J. Y. et al. Revival of Ferroelectric Memories Based on Emerging Fluorite-Structured Ferroelectrics. *Adv. Mater.* **35**, 2204904 (2023).
8. Kim, M. K. & Lee, J. S. Ferroelectric Analog Synaptic Transistors. *Nano Lett.* **19**, 2044–2050 (2019).
9. Das, D. & Khan, A. I. Ferroelectricity in CMOS-Compatible Hafnium Oxides: Reviving the Ferroelectric Field-Effect Transistor Technology. *IEEE Nanotechnol. Mag.* **15**, 20–32 (2021).
10. Schroeder, U., Park, M. H., Mikolajick, T. & Hwang, C. S. The Fundamentals and Applications of Ferroelectric HfO_2. *Nat. Rev. Mater.* **7**, 653–669 (2022).
11. Wang, Y. et al. A Stable Rhombohedral Phase in Ferroelectric $Hf(Zr)_{1+x}O_2$ Capacitor with Ultralow Coercive Field. *Science* **381**, 558–563 (2023).

12. Cheema, S. S. et al. Enhanced Ferroelectricity in Ultrathin Films Grown Directly on Silicon. *Nature* **580**, 478–482 (2020).
13. Böscke, T., Müller, J., Bräuhaus, D., Schröder, U. & Böttger, U. Ferroelectricity in Hafnium Oxide Thin Films. *Appl. Phys. Lett.* **99**, 102903 (2011).
14. Wang, L. et al. Effect of the Thickness of $BiFeO_3$ Layers on the Magnetic and Electric Properties of $BiFeO_3/La_{0.7}sr_{0.3}MnO_3$ Heterostructures. *Appl. Phys. Lett.* **102**, 242902 (2013).
15. Toriumi, A. et al. Material perspectives of HfO_2-based ferroelectric films for device applications. *Proc. IEEE Conf. Ser.* 15.1.1–15.1.4. (2019).
16. Park, M. H. et al. Understanding the Formation of the Metastable Ferroelectric Phase in Hafnia–Zirconia Solid Solution Thin Films. *Nanoscale* **10**, 716–725 (2018).
17. Zhu, T., Ma, L., Deng, S. & Liu, S. Progress in Computational Understanding of Ferroelectric Mechanisms in HfO_2. *npj Comput. Mater.* **10**, 188 (2024).
18. Zhou, Y. et al. The Effects of Oxygen Vacancies on Ferroelectric Phase Transition of HfO_2-Based Thin Film from First-Principle. *Comp. Mater. Sci.* **167**, 143–150 (2019).
19. Yan, F. et al. Recent Progress on Defect-Engineering in Ferroelectric HfO_2: The Next Step Forward Via Multiscale Structural Optimization. *Mater. Horiz.* **11**, 626–645 (2024).
20. Materlik, R., Künneth, C. & Kersch, A. The Origin of Ferroelectricity in $Hf_{1-X}Zr_xO_2$: A Computational Investigation and a Surface Energy Model. *J. Appl. Phys.* **117**, 134109 (2015).
21. Kang, S. et al. Highly Enhanced Ferroelectricity in HfO_2-Based Ferroelectric Thin Film by Light Ion Bombardment. *Science* **376**, 731–738 (2022).
22. Xu, X. et al. Kinetically Stabilized Ferroelectricity in Bulk Single-Crystalline HfO_2. *Y. Nat. Mater.* **20**, 826–832 (2021).
23. Yurchuk, E. et al. Impact of Layer Thickness on the Ferroelectric Behaviour of Silicon Doped Hafnium Oxide Thin Films. *Thin Solid Films* **533**, 88–92 (2013).
24. Park, M. H. et al. A Comprehensive Study on the Structural Evolution of HfO_2 Thin Films Doped with Various Dopants. *J. Mater. Chem. C.* **5**, 4677–4690 (2017).
25. Mittmann, T. et al. Impact of Iridium Oxide Electrodes on the Ferroelectric Phase of Thin $Hf_{0.5}Zr_{0.5}O2$ Films. *Phys. Status Solidi RRL-Rapid Res. Lett.* **15**, 2100012 (2021).
26. Park, M. H., Kim, H. J., Kim, Y. J., Moon, T. & Hwang, C. S. The Effects of Crystallographic Orientation and Strain of Thin $Hf_{0.5}Zr_{0.5}O_2$ Film on Its Ferroelectricity. *Appl. Phys. Lett.* **104**, 072901 (2014).
27. Qi, Y. et al. Stabilization of Competing Ferroelectric Phases of HfO_2 under Epitaxial Strain. *Phys. Rev. Lett.* **125**, 257603 (2020).
28. Yao, Y. et al. Experimental Evidence of Ferroelectricity in Calcium Doped Hafnium Oxide Thin Films. *J. Appl. Phys.* **126**, 154103 (2019).
29. Li, T. et al. Epitaxial Ferroelectric $Hf_{0.5}Zr_{0.5}O_2$ Thin Film on a Buffered YSZ Substrate through Interface Reaction. *J. Mater. Chem. C.* **6**, 9224–9231 (2018).
30. Materano, M. et al. Influence of Oxygen Content on the Structure and Reliability of Ferroelectric $Hf_XZr_{1-X}O_2$ Layers. *ACS Appl. Electron. Mater.* **2**, 3618–3626 (2020).
31. Lyu, J., Fina, I., Solanas, R., Fontcuberta, J. & Sánchez, F. O. Growth Window of Ferroelectric Epitaxial $Hf_{0.5}Zr_{0.5}O_2$ Thin Films. *ACS Appl. Electron. Mater.* **1**, 220–228 (2019).
32. Materano, M. et al. Interplay between Oxygen Defects and Dopants: Effect on Structure and Performance of HfO_2-Based Ferroelectrics. *Inorg. Chem. Front.* **8**, 2650–2672 (2021).
33. Pal, A. et al. Enhancing Ferroelectricity in Dopant-Free Hafnium Oxide. *Appl. Phys. Lett.* **110**, 022903 (2017).
34. Park, M. H. et al. Effect of Zr Content on the Wake-up Effect in $Hf_{1-X}Zr_XO_2$ Films. *ACS Appl. Mater. Interfaces* **8**, 15466–15475 (2016).
35. Yun, Y. et al. Intrinsic Ferroelectricity in Y-Doped HfO_2 Thin Films. *Nat. Mater.* **21**, 903–909 (2022).
36. Guo, J. et al. Rhombohedral R3 Phase of Mn-Doped $Hf_{0.5}Zr_{0.5}o_2$ Epitaxial Films with Robust Ferroelectricity. *Adv. Mater.* **36**, 2406038 (2024).
37. Uthra, B., Bang, V., Anantha, S. & Agarwal, P. B. Effect of Lanthanide Dopants on Stability of Orthorhombic Hafnium Oxide for Pyroelectric Applications. *Mater. Lett.* **317**, 132097 (2022).
38. Shi, S. et al. Stabilizing the Ferroelectric Phase of $Hf_{0.5}Zr_{0.5}O_2$ Thin Films by Charge Transfer. *Phys. Rev. Lett.* **133**, 036202 (2024).
39. Cao, T., Ren, G., Shao, D. F., Tsymbal, E. Y. & Mishra, R. Stabilizing Polar Phases in Binary Metal Oxides by Hole Doping. *Phys. Rev. Mater.* **7**, 044412 (2023).
40. Ma, L. Y. & Liu, S. Structural Polymorphism Kinetics Promoted by Charged Oxygen Vacancies in HfO_2. *Phys. Rev. Mater.* **130**, 096801 (2023).
41. Rijnders, G., Blank, D. H., Choi, J. & Eom, C. B. Enhanced Surface Diffusion through Termination Conversion during Epitaxial $SrRuO_3$ Growth. *Appl. Phys. Lett.* **84**, 505–507 (2004).
42. Shi, S. et al. Interface-Engineered Ferroelectricity of Epitaxial $Hf_{0.5}Zr_{0.5}O_2$ Thin Films. *Nat. Commun.* **14**, 1780 (2023).
43. Orvis, T. et al. Direct Observation and Control of Surface Termination in Perovskite Oxide Heterostructures. *Nano Lett.* **21**, 4160–4166 (2021).
44. Kresse, G. & Furthmüller, J. Efficient iterative schemes for ab initio total-energy calculations using a plane-wave basis set. *Phys. Rev. B* **54**, 11169 (1996).
45. Blöchl, P. E. Projector augmented-wave method. *Phys. Rev. B* **50**, 17953 (1994).
46. Giannozzi, P. et al. Advanced capabilities for materials modelling with Quantum ESPRESSO. *J. Phys. Condens. Matter* **29**, 465901 (2017).
47. Zheng, X. et al. Spatial defects nanoengineering for bipolar conductivity in MoS2. *Nat. Commun.* **11**, 3463 (2020).
48. Car, R. & Parrinello, M. Unified approach for molecular dynamics and density-functional theory. *Phys. Rev. Lett.* **55**, 2471–2474 (1985).
49. Vanderbilt, D. Soft self-consistent pseudopotentials in a generalized eigenvalue formalism. *Phys. Rev. B* **41**, 7892–7895 (1990).
50. Perdew, J. P., Burke, K. & Ernzerhof, M. Generalized gradient approximation made simple. *Phys. Rev. Lett.* **77**, 3865 (1996).
51. Henkelman, G., Uberuaga, B. P. & Jónsson, H. A climbing image nudged elastic band method for finding saddle points and minimum energy paths. *J. Chem. Phys.* **113**, 9901–9904 (2000).

Acknowledgements

This work is supported by the project of the National Natural Science Foundation of China (Program No. 12474061), the Natural Science Basic Research Program of Shaanxi (Program No. 2024JC-YBMS-009), Shaanxi Qinchuangyuan High-Level Innovative and Entrepreneurial Talent Introduction Program (QCYRCXM-2023-077), The Youth Project of "Shanxi High-level Talents Introduction Plan (5113240032)". Aviation Science Foundation 2021Z009053001, and Innovation Capability Support Program of Shaanxi (Program No. 2024RS-CXTD-30). Tengfei Cao also thanks Prof. Evgeny Tsymbal for the helpful discussions.

Author contributions

X.X.J., Y.H.Y., Z.W., T.F.C., Q.H., K.P.S., and S.N.L. contributed to the conceptualization and methodology. T.F.C. provided resources, project administration, supervision, and funding acquisition. X.X.J., Y.H.Y., and S.N.L. contributed to data curation. X.X.J., Y.H.Y., S.N.L., F.S., Z.K.Z., X.L.F., L.M.L., and S.F.W. were responsible for validation, formal analysis, and investigation. X.X.J., and Y.H.Y. contributed to visualization. Writing, including original draft preparation and review and editing, was carried out by X.X.J., Y.H.Y., J.K., S.N.L., X.H.Z., S.S., J.S.C., Z.W., and T.F.C.

Competing interests

The authors declare no competing interests.

Additional information

Supplementary information The online version contains supplementary material available at https://doi.org/10.1038/s42005-025-02438-x.

Correspondence and requests for materials should be addressed to Qi Hu, Xiaoli Fan, Zheng Wen or Tengfei Cao.

Peer review information *Communications Physics* thanks Gabriele De Luca and Shi Liu for their contribution to the peer review of this work.

Reprints and permissions information is available at http://www.nature.com/reprints

Publisher's note Springer Nature remains neutral with regard to jurisdictional claims in published maps and institutional affiliations.

Open Access This article is licensed under a Creative Commons Attribution 4.0 International License, which permits use, sharing, adaptation, distribution and reproduction in any medium or format, as long as you give appropriate credit to the original author(s) and the source, provide a link to the Creative Commons licence, and indicate if changes were made. The images or other third party material in this article are included in the article's Creative Commons licence, unless indicated otherwise in a credit line to the material. If material is not included in the article's Creative Commons licence and your intended use is not permitted by statutory regulation or exceeds the permitted use, you will need to obtain permission directly from the copyright holder. To view a copy of this licence, visit http://creativecommons.org/licenses/by/4.0/.

© The Author(s) 2025